Electronic Supplementary Material (ESI) for Catalysis Science & Technology.

Supplementary Information

1. Characterization techniques:

1.1 Powder X-Ray Diffraction (PXRD)

X-ray diffraction data of the samples were collected on a Philips PW1729 diffractometer operating in Bragg-Brentano focusing geometry and using CuK$_\alpha$ radiation (λ = 1.5418 Å) from a generator operating at 40 kV and 30 mA.

1.2 X-ray Photoelectron Spectroscopy (XPS)

XPS was performed using Kratos Ltd XSAM800.

1.3 Temperature Programed Reduction (TPR)

TPR was used to investigate the reduction behavior of catalysts and estimate the composition of produced metal particles. The data was collected on a Thermo-Quest TPRO 110 instrument. Inside the TPR quartz tube, 0.01 g of the calcined catalyst sample (at 300°C) was sandwiched between two layers of quartz wool with a thermocouple placed in contact with the top layer quartz wool. The TPR tube was then inserted into the instrument for a pre-treatment (helium running through the TPR tube at 10 mL min^{-1} at a temperature ramp of 10°C min^{-1} from 40°C up to 150°C, then held for 5 minutes before cooling). The helium pre-treatment cleaned the catalyst surface by removing the absorbed ambient gas molecules. After the pre-treatment, a reduction treatment (5% H_2 in argon flowing through the TPR tube at 20 mL min^{-1} at a temperature ramp of 10°C min^{-1} from 40°C up to 800°C) was carried out in order to observe the reduction process of the catalysts.

1.4 Extended X-ray Absorption Fine structure (EXAFS)

EXAFS measurements at Pd K-edge (24530 eV) were performed on beamline B18 at Diamond Light Source (Diamond, UK) to obtain information about the local structure of the noble metals (the nearest-neighbor inter-atomic distances and coordination number). Also, it was used to estimate the composition of metal particles. The Diamond installation comprises a 3 GeV electron storage ring with typical currents of 200 mA. B18 is a bending magnet beamline which has been designed to deliver monochromatic X-rays in the energy range of 2 to 35 keV. A Si (311) double crystal monochromator was used for energy selection with a resolution of 1 eV. X-ray absorption spectroscopy data were collected at ambient temperature in transmission mode using optimized ionization chambers as detectors. Fluorescence spectra were acquired using I_0 and a high count rate fluorescence 9-element Ge detector. The EXAFS data analysis was performed using IFEFFIT 1 with Horae packages 2 (Athena and Artemis). All spectra were calibrated with Pd foil as a reference to avoid small energy shifts of the nanocatalyst. The amplitude parameter was obtained from EXAFS data analysis of Pd foil with a known coordination number equals to 12, which was used as a fixed input parameter in all fits to allow coordination number (CN) refinement.

In this work, we have only performed a first shell data analysis under the assumption of a single scattering. The curve-fitting analyses were done in k^3 space with a range of 2-12. Errors in analysis were estimated by R-factor.

1.5 Transmission electron microscopy (TEM)

The shapes and size distributions of the nanocrystals were measured with a JEOL JEM 1230 transmission. The samples were prepared by placing a drop of nanoparticle-ethanol suspension onto a carbon-coated copper grid, then allowing the solvent to evaporate.

1.6 Computation method:

All calculations were performed in the framework of DFT by using the Vienna ab initio simulation package (VASP 4.6) [1-4]. The projector-augmented wave (PAW) potentials[5,6] were used for the core electron interaction. The Perdew–Burke–Ernzerhof (PBE) functional [7,8] based on the generalized gradient approximation(GGA) was employed to evaluate the non-local exchange-correlation energy. A plane wave basis set with a cutoff energy of 400 eV was used. For structure optimization, the ionic positions were allowed to relax until the forces were less than 0.05 eV/Å. Spin polarization is included for all the calculations.

2. Synthesis and characterization of cobalt blended Pd/Fe_2O_3 samples:

The synthesis procedure of cobalt blended Pd/Fe_2O_3 samples is described as followed: Iron oxide was used as main support of Pd particles and cobalt nitrate was added to act as the precursor of Co. Briefly, 1.55 g $Co(NO_3)_2.6H_2O$ and 7.59 g $Fe(NO_3)_3.9H_2O$ were dissolved in 50 mL and 200 mL water, separately (the ratio of Fe:Co in the final product is calculated to be 2.8). 10 mL Na_2CO_3 solution (1 M) was dropped to the solution containing Co precursor. The obtained white suspension was then dropped into the 200 mL $Fe(NO_3)_3$ solution and the pH of the final gel was adjusted to 4 by the Na_2CO_3 solution. The reddish gel was also added into 200mL $Pd(NO_3)_2$ (0.5 wt% Pd) solution and the pH of this mixture was adjusted to 9. The final mixture was left stirring overnight and the solid product was harvested by centrifugation. Samples were calcined at 300°C in air and then reduced with a flowing stream of hydrogen in a 3-neck flask at 250°C.

The concentration of Co in the final Pd-based bimetallic NPs can be tuned by the amount of cobalt precursor. With variable ratio of $Co(NO_3)_2$: $Fe(NO_3)_3$, a series of Pd samples with variable composition of support are synthesized and the details before pre-reduction are shown in Table S1.

Table S1. The compositions of a series of cobalt blended Pd/Fe_2O_3 samples before the pre-reduction.

Sample No.	Mass of added $Co(NO_3)_2.6H_2O$	Mass of added $Fe(NO_3)_3.9H_2O$	Calculated Co_3O_4:Fe_2O_3	Weight % of Co
1	0.00	9.61	0.00	0.00
2	1.55	7.59	0.19	16.28
3	2.36	6.54	0.33	24.58
4	3.50	5.06	0.64	36.01
5	5.05	3.04	1.54	51.30

(*Note: the calculation of Co weight % didn't take the amount of Pd into account, thus the value only represents the concentration of Co in the support*)

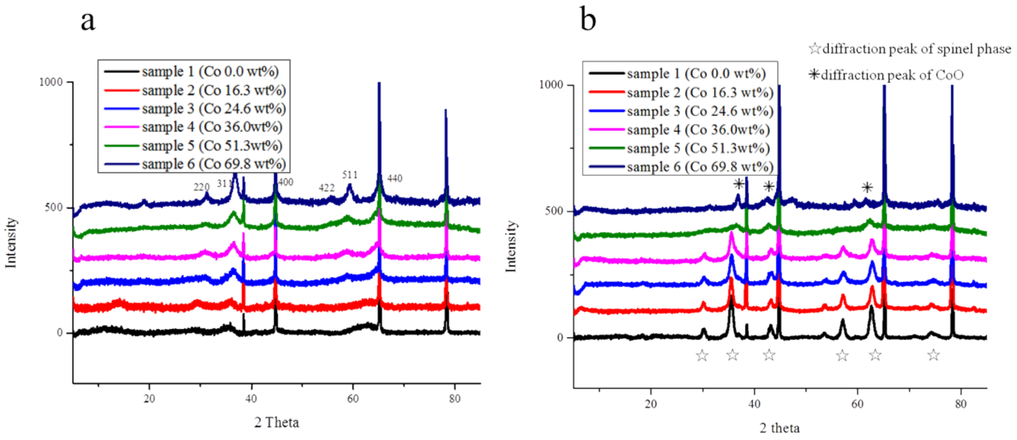

Fig. S1. XRD diffractograms of a series of Co(II) blended samples before pre-reduction.

XRD was conducted to characterize the lattice structure of the products. Fig. S1a displays the XRD diffractograms of the samples before pre-reduction. From sample 1 (without Co) to sample 6 (without Fe), the content of blended Co(II) increases continuously. However, there is no significant difference in the XRD peak positions. All the diffraction patterns can be indexed to a spinel structure. It is widely known that both γ- Fe_2O_3 and Co_3O_4 have a spinel structure in which oxygen ions are cubic close packed (CCP) while metal cations occupy 1/2 octahedral holes and 1/8 tetrahedral holes[9,10]. Thus, sample 1 is palladium supported on γ- Fe_2O_3 with no cobalt while sample 6 is palladium supported on Co_3O_4 (Some Co(II) was oxidized to Co(III) during the calcination in air). For sample 2 to sample 5, a series of mixtures of γ- Fe_2O_3 and Co_3O_4 at increasing Co content is obtained. However, due to the strongly overlapping of the diffraction patterns, no clear phase separation is observed.

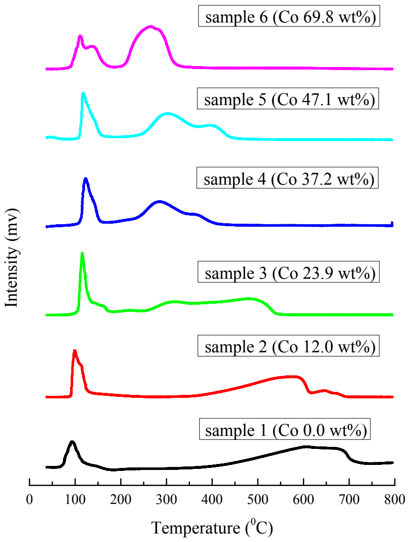

Fig. S2. TPR curves for a series of cobalt blended Pd/Fe_2O_3 samples.

In order to produce bimetallic cluster, the samples are pre-reduced at 250°C. Temperature programmed reduction (TPR) (Fig. S2) and X-ray diffraction (XRD) (Fig. S1b) are employed to investigate the reduction behavior and analyze the composition of reduced catalysts. As shown in Fig. S2, the two characteristic TPR peaks in sample 1 are mainly attributed to the stepwise reduction of iron oxide which are taken place in two steps: $Fe_2O_3 \rightarrow Fe_3O_4$ and $Fe_3O_4 \rightarrow Fe(0)$. PdO to Pd is known to readily take place at sub-ambient temperature. The second step is clearly taken place above 300°C corresponding to the second peak in TPR curves, while the first peak is related to the transformation of Fe_2O_3 to Fe_3O_4. The value of H_2 consumption (2.4 mmol g^{-1}) for the first peak around 100°C matches with the calculated theoretical value for the transformation of all the Fe_2O_3 to Fe_3O_4 (2.1 mmol g^{-1}) which means all the Fe_2O_3 in the support can be totally reduced to Fe_3O_4 during the pre-reduction temperature at 250°C. This deduction is supported by the result of XRD (Fig. S1b); all the diffraction peaks in the pattern of reduced sample 1 can be indexed to Fe_3O_4. For the TPR curve of sample 6 (palladium supported on Co_3O_4), two broad peaks are observed, the first one before 250°C refers to the catalytic reduction process of Co_3O_4 to CoO while the other one after 250°C is caused by the reduction of CoO to Co(0). Thus, the XRD diffractogram (Fig. S1b) of reduced sample 6 at 250°C reveals a typical rock salt structure, which is indexed to CoO[11]. For samples 2 to 5, the first catalytic reduction processes of mixed phases (Fe_2O_3 to Fe_3O_4 and Co_3O_4 to CoO) take place at similar temperature, so only one peak in the TPR before 250°C is observed. However, the H_2 consumptions of the first peak for all samples are consistently greater than the theoretical value needed to reduce the mixed phases (Fe_2O_3 to Fe_3O_4 and Co_3O_4 to CoO) when Co is added. This suggests that accompanying this reduction process, some surface CoO must have been further converted to Co(0) with the assistance of Pd(0). It can be understood that the reduction potential of Co(II) to Co(0) is more favourble than that of Fe(II) to Fe(0) [12,13] resulting in the selective formation of Co(0), which is also supported by the result of XPS (Fig. S3). Thus, with the calculated amount of H_2 consumption before 250°C from the integration area of peaks in TPR curves, the quantity of produced Co(0) for each sample can be obtained. The results are displayed in Table S2; it is noted that the amount of produced Co(0) varies with the content of blended Co(II) and reaches the peak at sample 4 as sample 4> sample 5 > sample 3 > sample 2. The volcano relationship is attributed to increase particle size of the support as shown in Fig. S1a at the increasing in Co content (the diffraction peaks of the support become narrower from sample 1(0.0 wt% Co) to sample 6 (69.8 wt% Co)). The increase in particle size reduces the contact interface with Pd. Consequently, the contradictory factors of the increasing amount of added Co precursor and the increasing particles size result in the volcano relationship between the produced Co(0) after reduction and the added Co(II) in the co-precipitation process.

Table S2. The calculated quantity of Co(0) from TPR for a series of $Pd/Co_3O_4/Fe_2O_3$ samples.

Sample No.	**2 (16.3wt% Co)**	**3 (24.6wt% Co)**	**4 (36.0 wt% Co)**	**5 (51.3wt% Co)**
H_2 consumption (mmol g^{-1})	3.9	5.1	6.0	6.1
Produced Co (mmol g^{-1})	1.6	2.5	2.9	2.8

(Note: the calculation of the amount of produced Co (0) is based on the following equation: N=(experimental H_2 consumption before 250 ℃) - (theoretical H_2 consumption of Fe_2O_3 to Fe_3O_4 and Co_3O_4 to CoO).)

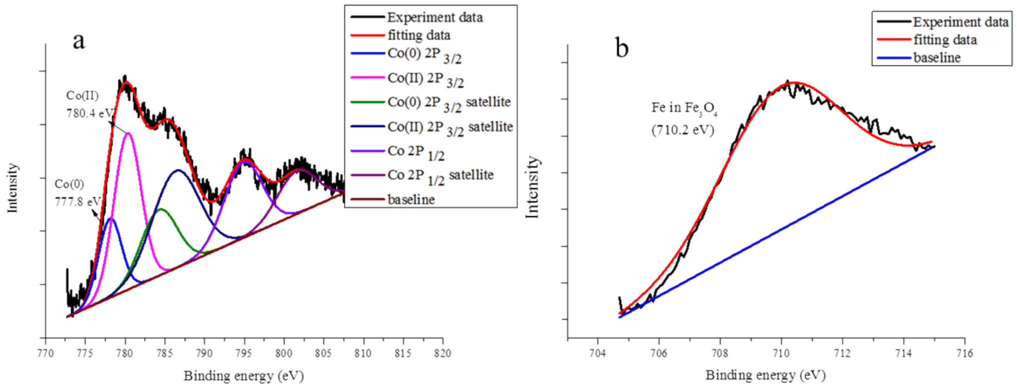

Fig. S3. XPS curves and the corresponding fitting results of a)Co and b)Fe in the reduced Pd/$CoFe_{2.8}O_x$ (sample 2 (Co 16.3 wt%))

Fig. S3 displays the XPS curves of cobalt and iron for reduced sample 2(Co 16.3 wt%). Two groups of peaks are observed in the spectroscopy of Co (Fig. S3a); the one located around 780 eV is assigned to the $2P_{3/2}$ peak of Co accompanied by its satellite peak (786 eV), the other one at 795 eV corresponds to $2P_{1/2}$ peak of Co which is also followed by the satellite peak (803 eV)[14]. The $2P_{3/2}$ peak of Co can be evidently fitted into 2 peaks; one is located at 780.4 eV corresponding to the signal of Co(II) while the other one is around 777.8 eV which can be clearly assigned to the signal of Co(0) [15]. The intense peak at 777.8 eV indicates a significant proportion of Co(0) in the catalyst. Whereas from the curve of Fe (Fig. S3b), a binding energy of 710.2 eV is observed which is consistent with the literature value of Fe_3O_4 indicating the preference H_2 reduction of Co(II) to Co(0) which gives a less negative reduction potential than Fe(II) to Fe(0).

The (XPS) curves of cobalt for a series of reduced samples are displayed in Fig. S4. With the increasing content of Co(II), more Co(0) atoms are produced in the reduction process, and the corresponding Co(0) $2P_{3/2}$ signal in XPS grows which reaches the peak at sample 4 and it is consistent with the results of TPR. The change of XPS signal of Co(0) indicates the successful control of Co concentration in the active site of the catalysts.

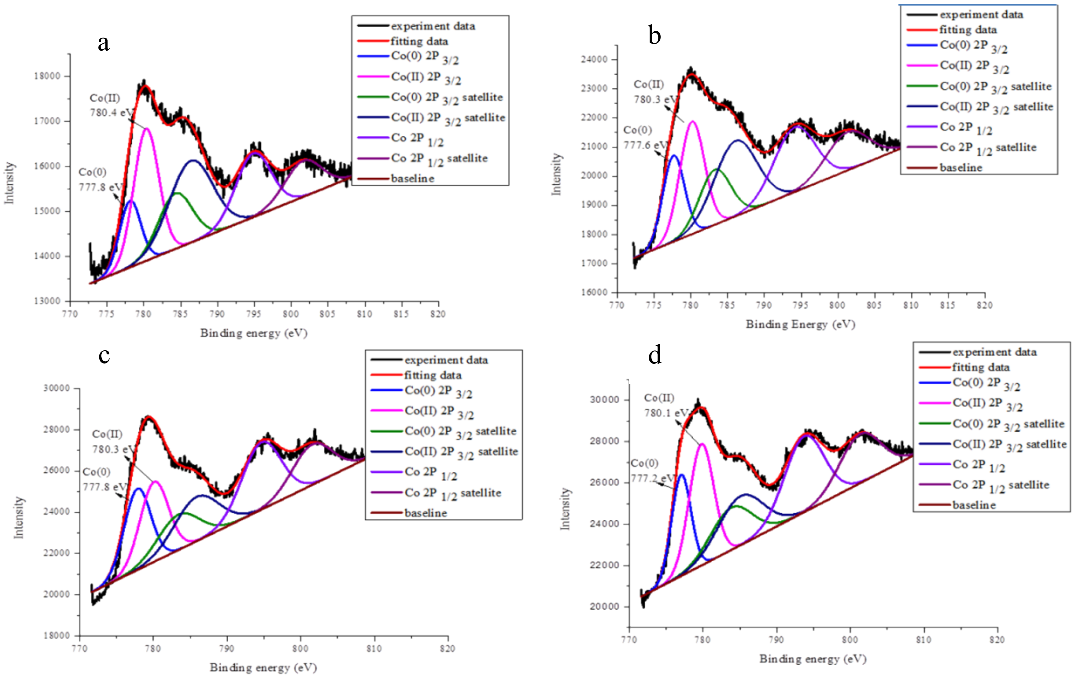

Fig. S4. XPS curves of Co in a) sample 2 **(**16.3 wt% Co); b) sample 3 **(**24.6 wt% Co); c) sample 4 **(**36.0 wt% Co); d) sample 5 **(**51.3 wt% Co) after the pre-reduction.

The formation of PdCo alloy was confirmed by the results of EXAFS shown the Fig. 1 and the content of Co is well controlled by the tuning of SMSI through careful variation of the support. The detailed coordination environment of the Pd is summarized in Table S3. The corresponding fitting curves of Pd in k^3 space for a series of reduced PdCo samples are shown in Fig. S5. The experimental curves and the fitting result match well with each other indicating the reliability of the derived data.

Table S3. Average coordination environment of a Pd atom from EXAFS of a series of PdCo samples

Sample Number	Total CN	Enot(eV)	Pd-Pd distance (Å)	D-W factor(Å^2)	Pd-Co distance (Å)	D-W factor(Å^2)	R-factor
2	6.8(4)	1.2	2.69(1)	0.010(1)	2.58(1)	0.010(1)	0.4%
3	7.2(7)	-2.2	2.70(1)	0.013(2)	2.57(1)	0.005(1)	0.8%
4	7.3(7)	-3.8	2.71(1).	0.010(1)	2.55(1)	0.006(1)	0.6%
5	7.9(5)	-3.6	2.70(1)	0.008(1)	2.58(1)	0.012(1)	0.4%

(“CN” is coordination number; “enot” is the energy difference between the experimental absorption energy and the calculated value in curve fitting; “D-W” is Debye Waller; “R factor” is the indication of the quality of curve fitting)

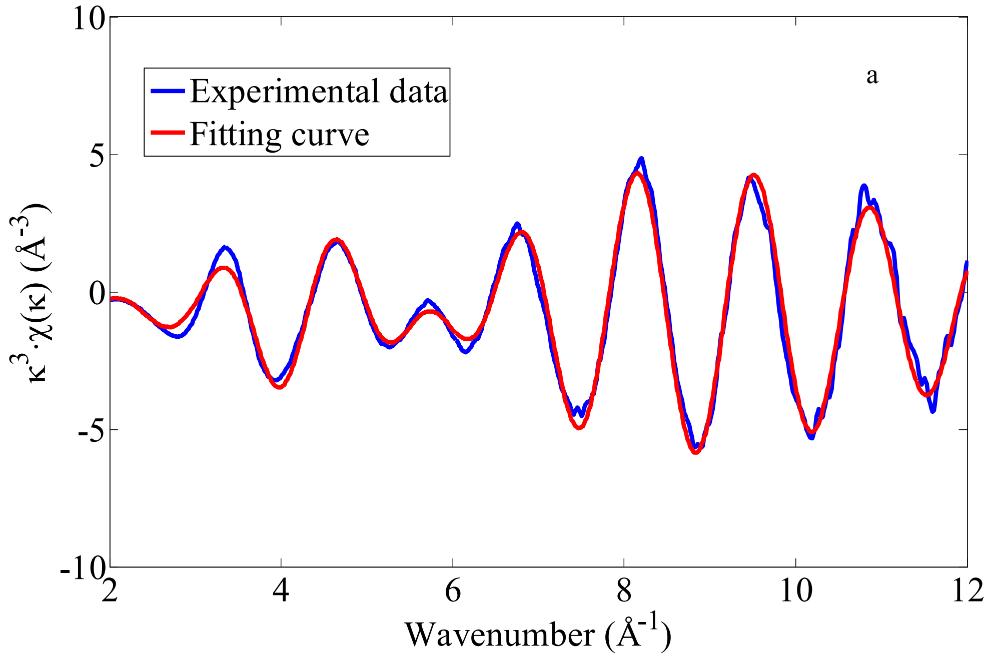
a
Experimental data
Fitting curve
$\kappa^3\cdot\chi(\kappa)$ (Å^{-3})
10
5
0
-5
-10
2
4
6
8
10
12
Wavenumber (Å^{-1})

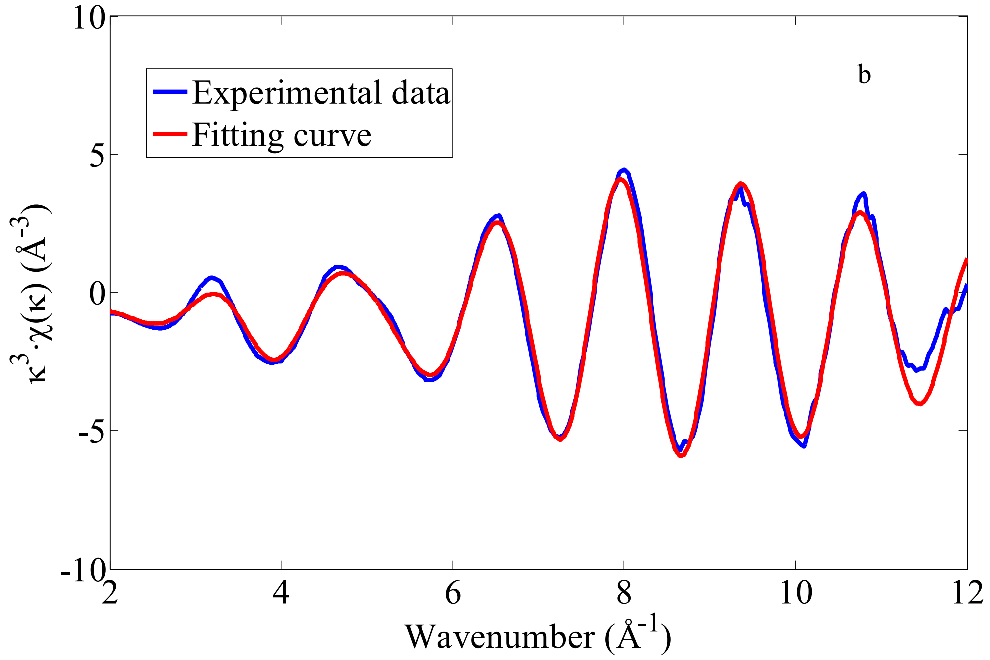
b
Experimental data
Fitting curve
$\kappa^3\cdot\chi(\kappa)$ (Å^{-3})
10
5
0
-5
-10
2
4
6
8
10
12
Wavenumber (Å^{-1})

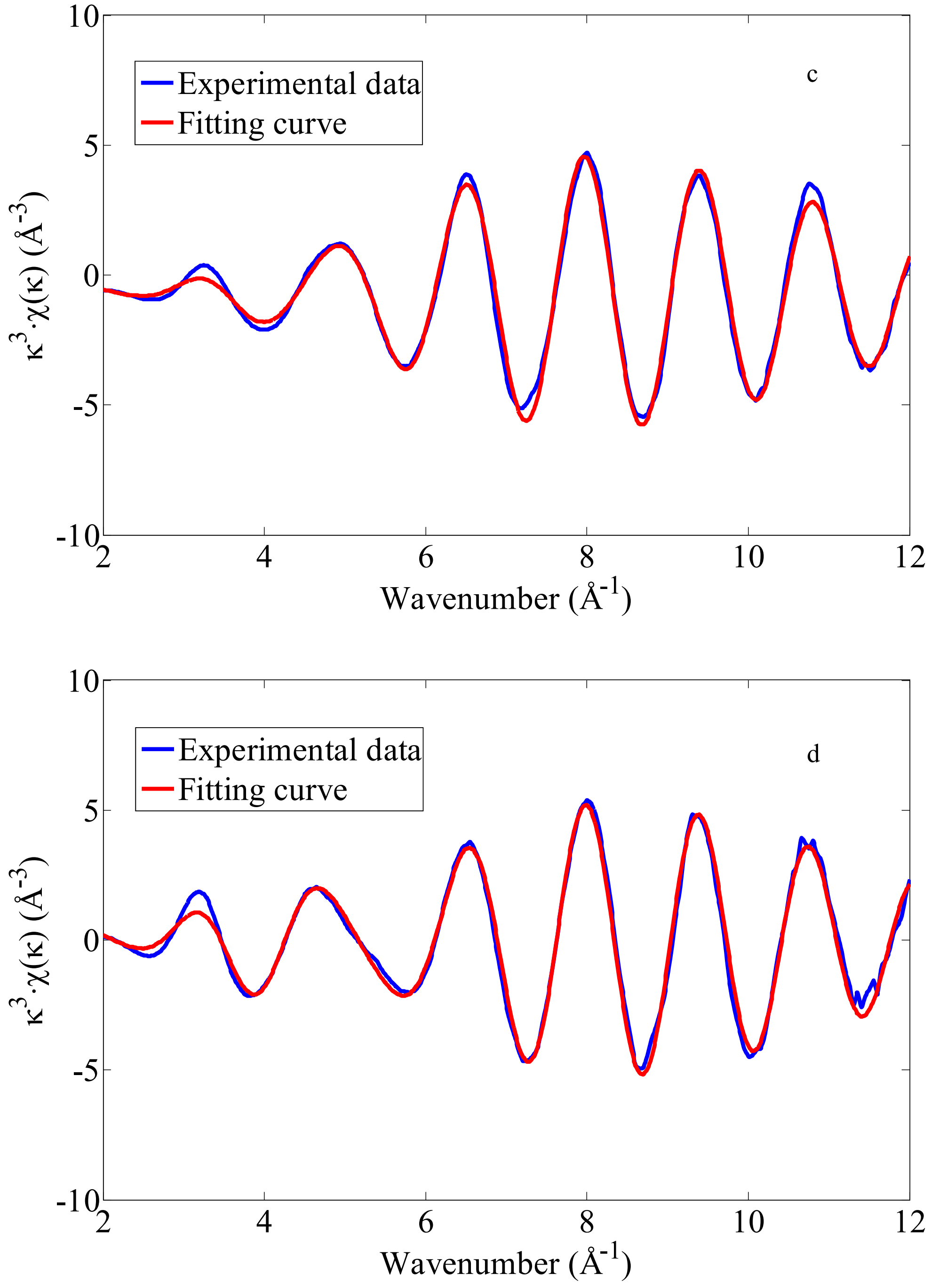

Fig. S5. k^3 space EXAFS curves of Pd in a R range of 2-12 for a series of reduced PdCo samples: a) sample 2 (16.3 wt% Co), b) sample 3 (24.6 wt% Co), c) sample 4 (36.0 wt% Co), d) sample 5 (51.3 wt% Co). (blue: experiment data; red: fitting data)

Transmission electron microscopy (TEM) was conducted to acquire the detailed microscopic view for the PdCo particles and the results are displayed in Fig. S6. In these samples, a large number of small bimetallic particles are observed to be dispersed on the support; the size ranged from ca. 0.8 to 2.4 nm in diameter, with particles of 1.5 nm being the most commonly measured size, which is consistent with estimation from the results of EXAFS. It also suggests the different amount of blended Co(II) does not influence the particle size significantly.

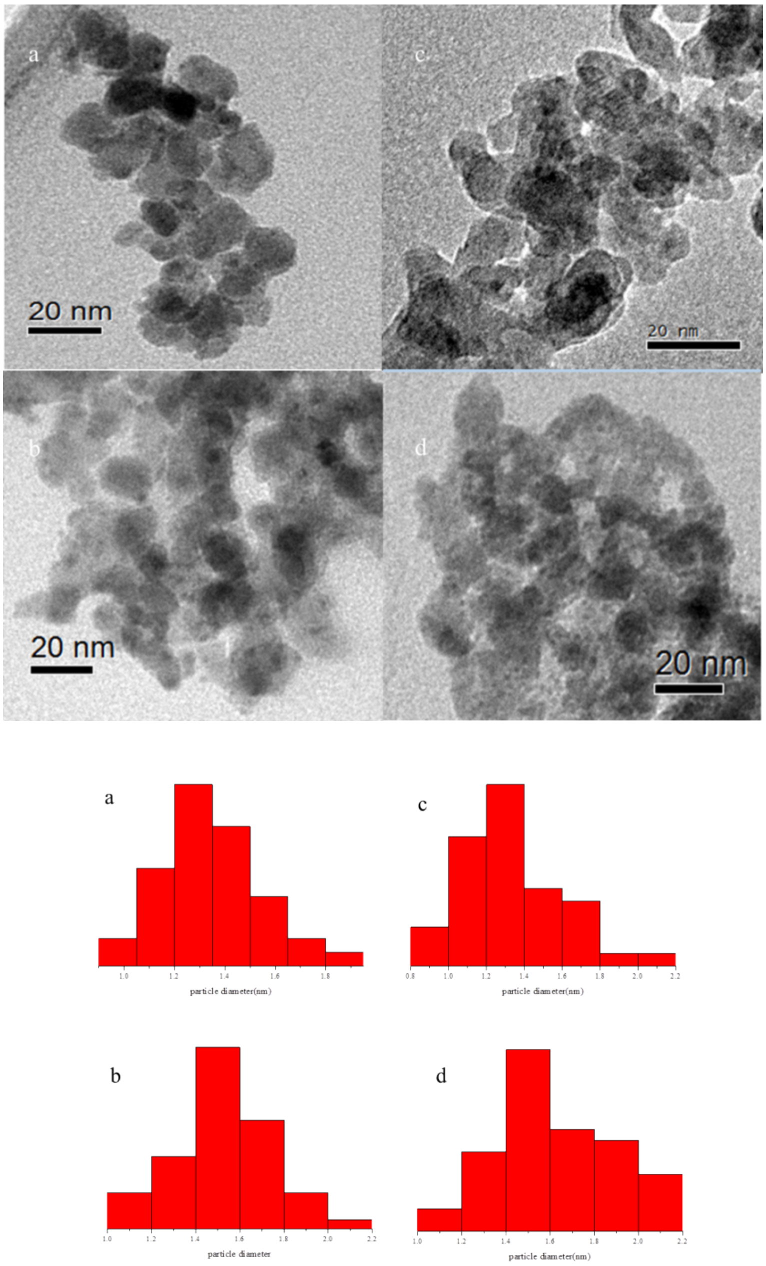

Fig. S6. Top) TEM images of reduced a) sample 2 (16.3 wt% Co), b) sample 3 (24.6 wt% Co), c) sample 4 (36.0 wt% Co), d) sample 5(51.3 wt% Co). Below) Pd particle size distribution in a) sample 2(16.3 wt% Co), b) sample 3(24.6 wt% Co), c) sample 4 (36.0 wt% Co), d) sample 5 (51.3 wt% Co).

3. Computation of the d-band structure of a series of PdCo alloys.

To study the concentration effects of Co modification, a simple model of non-segregated surface alloy was used here (the composition of PdM bulk alloy model cannot be set freely due to the consideration of symmetry for the calculation although it can reflect the structure of alloy better than this simple surface substitution model). Various amount of Co impurities were induced to substitute for surface Pd atoms on Pd(111) as showed in Fig. S7. The k-point grid determined by the Monkhorst-Pack method was 5×5×1. The Calculated Surface Density of states (SDOS) diagrams are shown in Fig. S8; the density of states clearly shifts to a higher position with the increasing concentration of Co due to the higher energy level of Co 3d than that of Pd 4d.

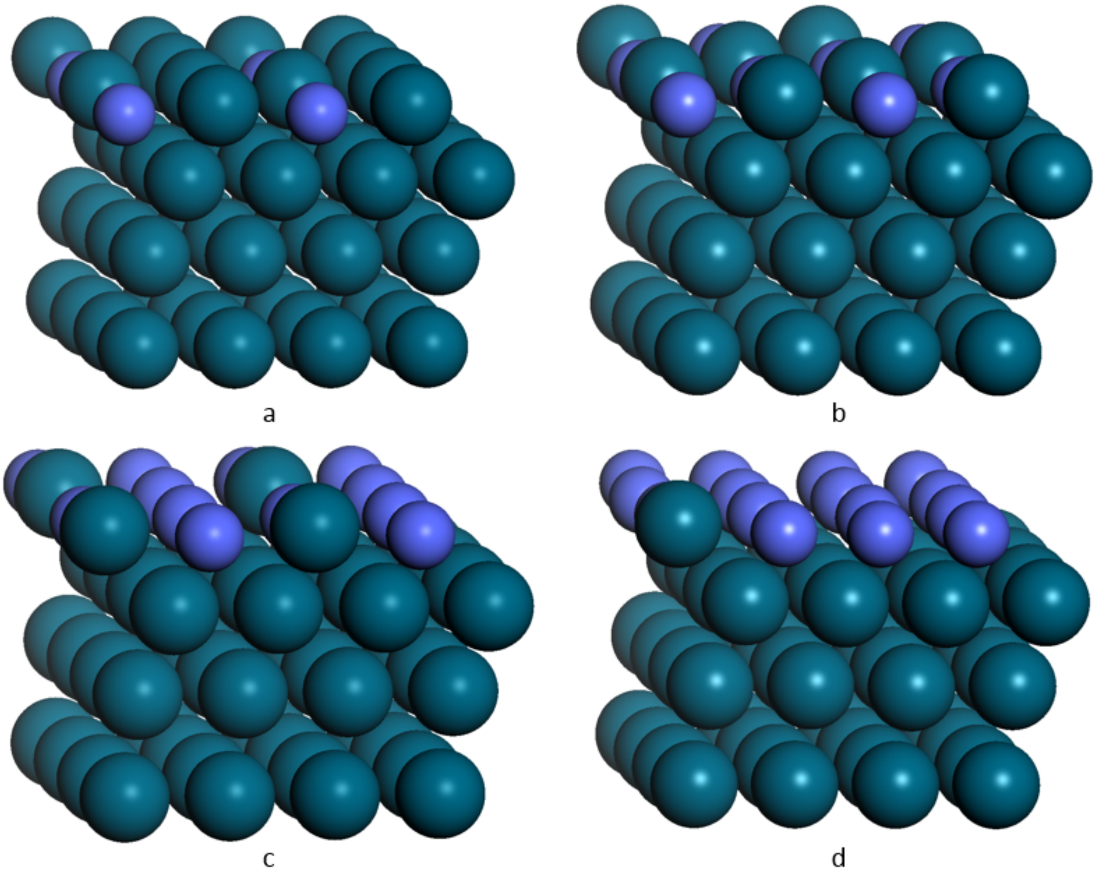

Fig. S7. surface alloy models of a)Pd_3Co; b)PdCo; c)$PdCo_3$; d) $PdCo_{15}$ (Blue balls represent Pd atoms and purple balls are Co atoms, the structure of $Pd_{15}Co$ is the same with Fig. S7d but only shows opposite position of Pd and Co on the surface layer)

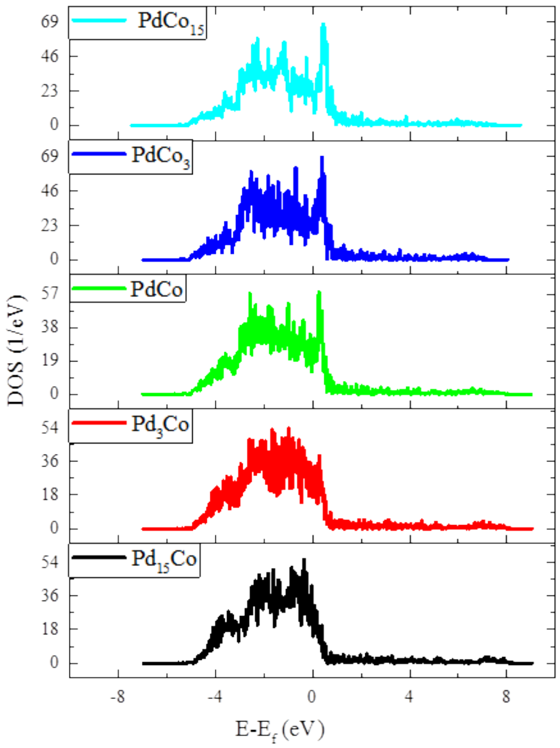

Fig. S8. Calculated Surface Density of states (SDOS) diagrams of a series of PdCo alloys with variable composition.

4. Synthesis and characterizations of a series of PdM (M=Fe, Co, Ni and Zn)

The successful synthesis of supported PdFe, PdNi and PdZn NPs was achieved by varying the corresponding support with the same Pd loading, followed by a H_2 reduction.

The synthesis of PdFe and PdNi catalyst is similar with that of PdCo, which is described as followed; 1.48 g $M(NO_3)_2.6H_2O$ (M=Zn for the synthesis of PdFe, M=Ni for the synthesis of PdNi) and 7.50 g $Fe(NO_3)_3.9H_2O$ were dissolved into 50 mL and 200 mL distilled water, respectively. 10 mL Na_2CO_3 solution (1 M) was dropped to the $M(NO_3)_2$ solution to produce a white suspension. The obtained mixture was then added dropwise into the 200 mL $Fe(NO_3)_3$ solution to form a reddish gel-like solution. The pH of the final gel was adjusted to 4 by adding 1 M Na_2CO_3 solution. Then, the reddish gel was added slowly into a solution of 200mL $Pd(NO_3)_2$ (0.5 wt% Pd), and the pH of this mixture was adjusted to 9 by adding more 1 M Na_2CO_3 solution. The final mixture was left stirring overnight and the solid product was harvested by centrifugation. The calcination and pre-reduction process is the same with that of PdCo sample.

The PdZn catalyst is produced by a typical co-precipitation method. [16] 0.6618g $Pd(NO_3)_2$ solution (15 wt% Pd) and 7.4g zinc nitrate $[Zn(NO_3)_2 . 6H_2O]$ were dissolved in 400ml deionized water. 1M Na_2CO_3 solution was dropped to precipitate Zn^{2+} and Pd^{2+} until the PH of the mixture reached 9. The crystalline product was then collected by centrifuged and was washed with deionized water for 10 times. The final product was dried in an oven at 60 °C for 12 hours. The final product is calcined and pre-reduced at the same condition with PdFe and PdCo sample.

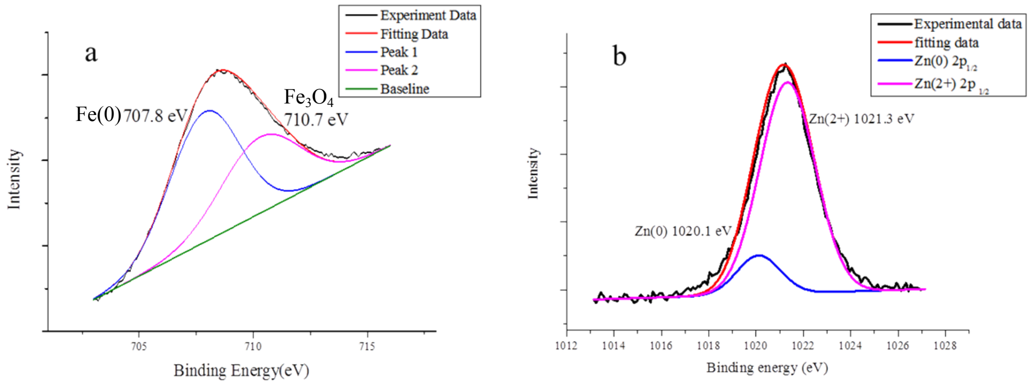

Fig. S9. XPS curves and the corresponding fitting results of a) Fe, b) Zn in the reduced Pd/FeO_x and Pd/ZnO_x, respectively

As shown in Fig. S9, the XPS curves of both Fe and Zn can be fitted into 2 peaks. As previously reported [17,18], the ones with higher binding energy (710.7 eV and 1021.3 eV) is assigned to the signal of Fe_3O_4 and ZnO, respectively. Meanwhile, the peaks at 707.8 eV and 1020.1 eV account for the existence of metallic Fe and Zn, which implies the reduction of the oxides to their metallic states.

The formations of PdM (M=Fe, Co, Ni, Zn) are also confirmed by EXAFS. The detailed (EXAFS) fitting results of the catalysts are summarized in Table S4.

Table S4(a). Total coordination number of a Pd absorbing atom, R factor and Enot value of each fitting in PdFe, PdCo, PdNi and PdZn clusters

Sample	Total CN	R factor	Enot (eV)
PdFe	5.8(6)	2.7%	-0.8
PdCo	6.8(4)	0.4%	1.2
PdNi	6.3(5)	1.1%	-7.8
PdZn	6.3(7)	2.4%	-5.0

Table S4(b). Average coordination environment of a Pd absorbing atom for the PdFe, PdCo, PdNi, PdZn from the EXAFS result

Sample	Scatting pair	Bond length (Å)	CN	D-W factor(Å^2)
PdFe	Pd-Pd	2.69(1)	3.9(4)	0.011(1)
	Pd-Fe	2.57(1)	1.9(2)	0.010(1)
PdCo	Pd-Pd	2.69(1)	4.8(2)	0.010(1)
	Pd-Co	2.58(1)	2.0(2)	0.010(1)
PdZn	Pd-Pd	2.70(1)	4.0(5)	0.012(1)
	Pd-Zn	2.56(1)	2.3(2)	0.004(2)
PdNi	Pd-Pd	N.A.	0	N.A.
	Pd-Ni	2.56(1)	6.3(5)	0.007(1)

("CN" is coordination number; "enot" is the energy difference between the experimental absorption energy and the calculated value in curve fitting; "D-W" is Debye Waller; "R factor" is the indication of the quality of curve fitting)

As shown in Table S4, all the R factors for EXAFS fittings are below 3% indicating the reliability of the results. The presence of first shell neighbor M (where M = Fe, Co, Zn) around each Pd adsorbing atom indicates successful synthesis of PdFe, PdCo and PdZn bimetallic clusters. However, in PdNi sample, no Pd-Pd scattering path is observed which implies the much higher concentration of Ni in the alloy than that of the other transition metal in PdM. The failure of controllable synthesis of PdNi for the systematic comparison among PdM alloys is presumably due to the fast reduction of Ni(II) to Ni(0).

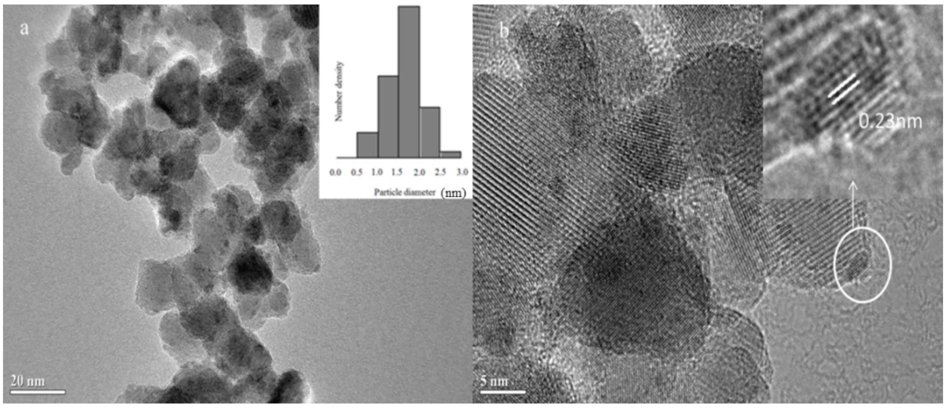

c d

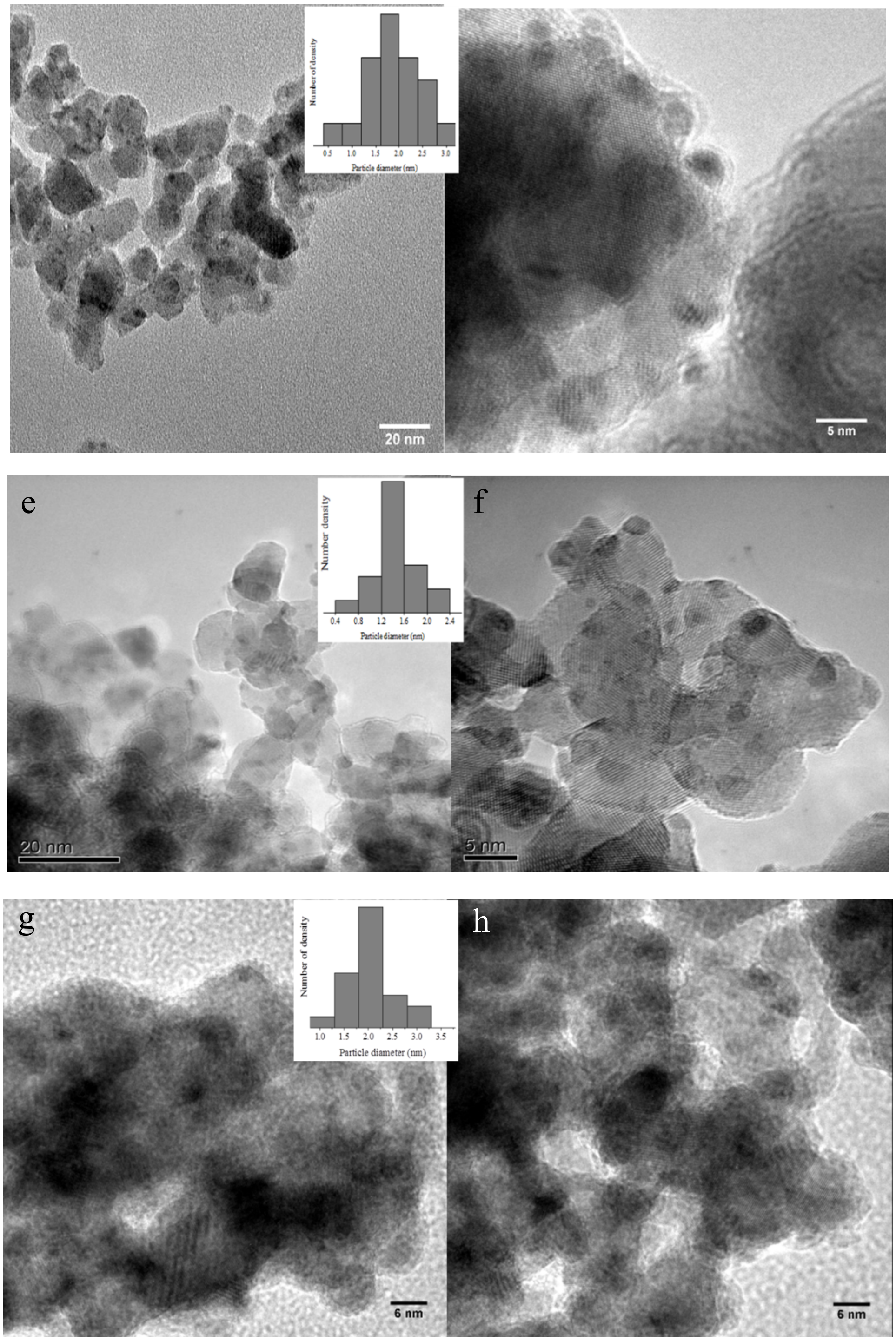

Fig. S10 TEM and HRTEM of supported PdFe (a, b), PdCo (c, d), PdZn (e, f) particles with NM around 2(M=Fe, Co, Zn) and PdNi(g, h),NNi=6.3.

The typical TEM images of supported PdM (M=Fe, Co, Zn, Ni) are shown in Fig. S10; a clear lattice fringe of 0.23nm is observed on the surface of the sample (Fig. S10b), which should be assigned to (111) plane of Pd-based particle [19]. The particle size in all the samples ranged from ca. 0.5 to 2.5 nm in diameter, with particles of 1.0 to 2.0 nm being the most commonly measured size which is consistent with the results of EXAFS and indicative of the similar particle size among the PdM particles.

5. Catalyst testing: Hydrogenolysis of ethylene glycol in a liquid phase batch reactor

The hydrogenolysis reaction was carried out in liquid phase using a 160 mL autoclave. In a typical experiment, 30 mL of ethylene glycol solution (0.85 mol L^{-1}) and 0.50 g catalyst were loaded into the reactor inside a glove box. The reactor was flushed with pure hydrogen gas to remove any trace of air. The autoclave was pressurized to 50 bar with hydrogen gas at room temperature, after which it was heated up to 250°C to allow the reaction to proceed for 24 hours with constant stirring. After the reaction, the autoclave was cooled down to -60°C by dry ice / acetone bath. Subsequently, the gas phase was analyzed by a Perkin Elmer Autosystem XL Arnel Gas Phase GC-FID-Methanator to determine the concentrations of CO, CH_4 and CO_2. The liquid phase was analyzed by a Perkin Elmer 200 series HPLC equipped with a refractive index detector. A 0.60 mL 58 mmol L^{-1} sucrose solution was added as an external standard to determinate the concentration of ethylene glycol, methanol and ethanol. The catalytic performance of supported PdM sample with variable compositions is displayed in Table S5 and Table S6

.**Table S5a.** Catalytic performance of a series of supported PdCo samples in the hydrogenolysis of ethylene glycol (EG) (0.50 g catalyst; 30 mL of EG solution (5 wt%); 50 bar H_2 (r.t.); temp. = 250 °C for 24 h)

Catalyst (5 wt% Pd)	**Conv%**	**Select.% CH_3OH**	**Select.% C_2H_5OH**	**Select.% CO_2**	**Select.% CH_4**	**Select. cleave of C-O/C-C**	**Select.% total alcohols**
Sample 2 (16.3 wt% Co)	31.2	35.9	12.7	30.9	18.7	0.35	48.6
Sample 3 (24.6 wt% Co)	34.2	19.0	23.8	37.8	18.5	1.25	41.8
Sample 4 (36.0 wt% Co)	25.3	14.3	51.1	21.7	12.3	3.57	65.4
Sample 5 (51.3 wt% Co)	20.7	13.1	46.2	21.3	18.4	3.53	59.3

Table S5b. Optimization of sample 4 (36.0 wt% Co) in hydrogenolysis of ethylene glycol (EG) with variable temperature (0.50 g catalyst; 30 mL of EG solution (5 wt%); 50 bar H_2 (r.t.) for 24 h)

Temperature (°C)	**Conv%**	**Select.% CH_3OH**	**Select.% C_2H_5OH**	**Select.% CO_2**	**Select.% CH_4**	**Select. cleave of C-O/C-C**	**Select.% total alcohols**
250	25.3	14.3	51.1	21.7	12.3	3.57	65.4
245	11.0	13.0	51.0	16.3	19.4	3.92	64.0
240	6.2	11.4	60.3	14.7	12.5	5.29	71.7
235	5.8	8.0	67.0	9.7	14.7	8.37	75.0

Table S5c. Optimization of sample 4 (36.0 wt% Co) in hydrogenolysis of ethylene glycol (EG) with variable mole ratio of Pd catalyst: substrate (30 mL of EG solution (5 wt%); variable amount of catalyst; 50 bar H_2 (r.t.); temp= 240℃ for 24 h))

Mole ratio of Pd:EG	**Conv%**	**Select.% CH_3OH**	**Select.% C_2H_5OH**	**Select.% CO_2**	**Select.% CH_4**	**Select. cleave of C-O/C-C**	**Select.% total alcohols**
0.005	4.7	14.6	44.0	23.2	16.6	3.01	65.4
0.010	6.2	11.4	60.3	14.7	12.5	5.29	71.7
0.015	13.4	6.0	67.0	20.9	5.1	11.17	73.0
0.020	35.2	8.6	70.0	18.2	3.4	8.14	78.6
0.020*	4.0	1.2	91.7	4.2	1.8	76.42	92.9

*reaction time= 8h

Through optimization of the reaction condition for sample 4 (36.0 wt%), it is observed that the ethanol selectively generally rises with the downshift of reaction temperature and also with the increasing amount of catalyst corresponding to an increasing ratio of noble metal catalyst to substrate (EG). A 70% ethanol selectivity with a high value of "selective cleavage of C-O: selective cleavage of C-C" over 8 can be achieved (total alcohol selectivity of 80%) at high conversion (35.2%). A short reaction time by quenching the reactor after 8 hour reaction (steady state conversion may not have been reached) can produce the highest ethanol selectivity (91.7%) but the conversion is low. Methanol and ethanol appear to be the primary products in hydrogenolysis of ethylene glycol. The higher ethanol selectivity at higher catalyst ratios may suggest faster kinetics for ethanol production than methanol (could be lying on the rate of product desorption) when a larger amount of catalyst is provided but more detailed kinetic studies at much low substrate conversions under differential reactor conditions are required.

Table S6a. Catalytic performance of PdFe, PdCo and PdZn bimetallic nanoparticles in hydrogenolysis of ethylene glycol (0.50 g catalyst; 30 mL of EG (5 wt%); 50 bar H_2 (r.t.); temp. = 250 °C for 24 h)

Active site	**Conv. %**	**Select.% CH_3OH**	**Select.% C_2H_5OH**	**Select.% CO_2**	**Select.% CH_4**	**Select. cleavage of C-O/C-C**
PdFe	25.0	50.1	3.0	45.1	1.2	0.06
PdCo	31.2	35.9	12.7	30.9	18.7	0.36
PdZn	4.6	18.6	23.6	56.8	0.4	1.27

Table S6b catalytic performance of supported PdNi sample in the hydrogenolysis of ethylene glycol (0.50 g catalyst; 30 mL of EG (5 wt%); 50 bar H_2 (r.t.); temp. = 250 °C for 24 h)

Active site	**Conv%**	**Select.% CH_3OH**	**Select.% C_2H_5OH**	**Select.% CO_2**	**Select.% CH_4**	**Select. cleave of C-O/C-C**
PdNi	54.8	12.7	12.8	1.5	73.0	1.01

6. Computation of the d-band structures of PdFe, PdCo, PdNi and PdZn:

As showed in Fig. S11, Pd_3M (M=Fe, Co, Zn) antisegregation bulk alloy models are conducted to investigate the effect of secondary element on the d-band filling of Pd which are similar to previous studies[20-27]. In these models, the Pd atoms occupy the face-centerd positions while the M metal atoms replace the corners so the ratio of Pd:M is 3:1 in the unit cell. The k-point grid determined by the Monkhorst-Pack method was 16×16×16. The lattice parameters, which were obtained after a bulk optimization for each alloy, are listed in Table S7. The most abundant close-packed $Pd_3M(111)$ surface was modeled by a periodic slab model with four layers of metals. The alloy atoms in the top layer were exchanged to the second layer. A 4×4 surface unit cell was used and the bottom layer was fixed during all geometry optimizations. A vacuum layer of 15 Å along the z direction perpendicular to the surface (the x and y directions being parallel to the surface) was employed to prevent spurious interactions between the repeated slabs. The corresponding calculated Surface Density of States (SDOS) diagrams for the Pd_3M alloys are shown in Fig. S12.

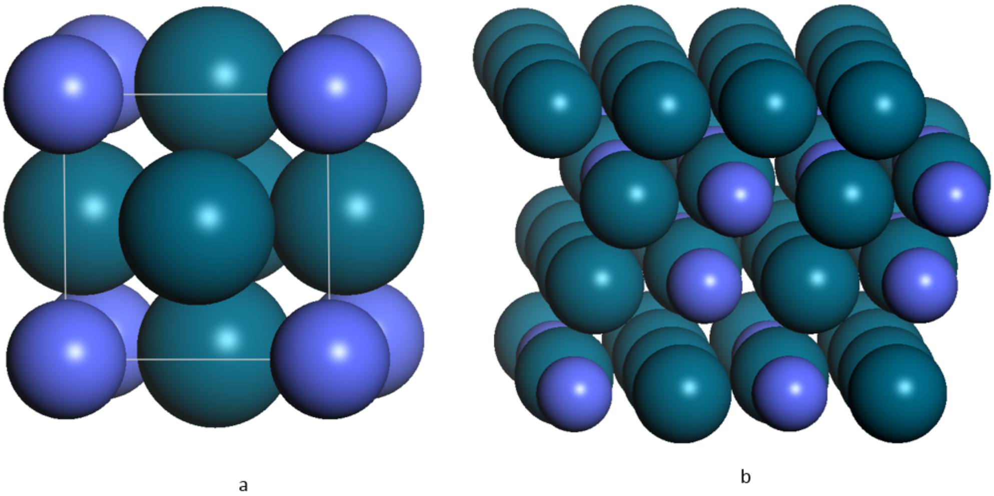

Fig. S11. a)Pd_3M bulk alloy model and b)close packed (111) surface model (Blue balls represent Pd atoms and purple balls are secondary atoms (Fe, Co, Zn))

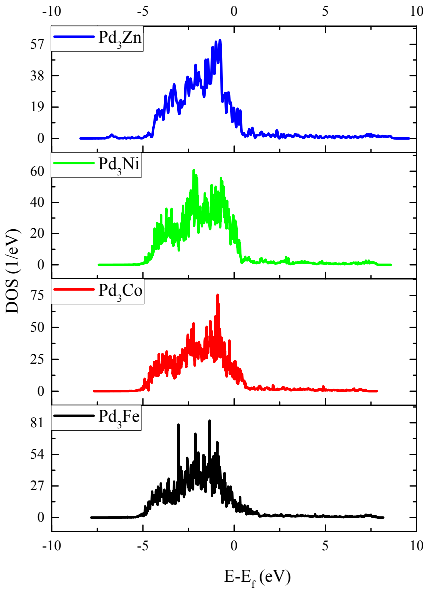

Fig. S12. Calculated Surface Density of states (SDOS) diagrams of PdFe, PdCo, PdNi, PdZn

Table S7. Typical lattice parameters of Pd_3M alloys

M element in Pd_3M	Bulk lattice parameter (Å)	Surface 2D parameter (Å)
Pd	3.952	11.179
Fe	3.891	11.005
Co	3.872	10.952
Ni	3.899	11.028
Zn	3.916	11.076

The lattice parameters of the Pd_3M (M=Fe, Co, Zn) alloy models were obtained after a bulk optimization. As shown in Table S7, the value of Pd_3Zn alloy is higher than those of Pd_3Co and Pd_3Fe which is consistent with the result of EXAFS shown in Table S4 (the distance of Pd-Pd in PdZn is longer than those in PdFe and PdCo). A longer distance between neighbor Pd atoms leads to a weaker overlap of the d orbitals which cause an up-shift in d-band center position and this explains the higher value of d-band center position for PdZn alloy as shown in Fig. 4a.

Due to the relatively high reduction potential of Ni(II) to Ni(0) (E^0[Ni(2+)/Ni(0)] = -0.25 eV), the reduction behavior of Ni(II) is uncontrollable and the concentration of Ni(0) in the PdNi bimetallic cluster is much higher than the other secondary atoms. Thus, the calculation model used for the PdCo alloy with variable composition is also applied to investigate the d-band structure of PdNi in a wide range of Ni content and the result is shown in Table S8 .

Table S8. Calculated d-band structure of Pd in a series of PdNi bimetallic nanoparticles with variable composition

Sample	d-band filling	Surface d-band center (eV)
Pd	0.88	-1.36
Ni_1Pd_{15}	0.88	-1.28
Ni_1Pd_3	0.88	-1.24
Ni_1Pd_1	0.87	-1.12
Ni_3Pd_1	0.88	-1.06

As shown above, the d-band filling of PdNi is kept at 0.88, due to the same number of valence electrons in Pd and Ni. But the Pd d-band center position rises with the increasing concentration of Ni.

A final remark of this work

It is well accepted that the acid-base properties of support can influence the adsorption and activation of EG but was not the main focus of the studied parameter in this paper, which should be studied in detail for the optimization of the catalytic reaction. We have seen no evidence on the formation of tri-metal PdFeM alloy under working conditions but cannot be ruled out the trace quantity at the material interface.

Reference:

[1] Kresse G.and Hafner J. , Ab initio molecular dynamics for liquid metals. *Phys. Rev. B.* **47,** 558-561(1993).

[2] Kresse G.and Hafner J., Ab initio molecular-dynamics simulation of the liquid-metal-amorphous-semiconductor transition in germanium. *Phys. Rev. B.* **49,** 14251-14269(1994)

[3] Kresse G. and Furthmüller J., Efficiency of ab-initio total energy calculations for metals and semiconductors using a plane-wave basis set. *Comput. Mat. Sci.* **6,** 15-50(1996).

[4] Kresse G. and Furthmüller J., Efficient iterative schemes for ab initio total-energy calculations using a plane-wave basis set. *Phys. Rev. B.* **54,** 11169-11186(1996).

[5] Blochl P. E., Projector augmented-wave method. *Phys. Rev. B.* **50,** 17953-17979(1994)

[6] Kresse G. and Joubert D., From ultrasoftpseudopotentials to the projector augmented-wave method. *Phys. Rev. B.* **59,** 1758-1775(1999).

[7] Perdew J. P., Burke K., and Ernzerhof M., Generalized gradient approximation made simple. *Phys. Rev. Lett.* **77,** 3865-3868(1996).

[8] Perdew J. P., Burke K., and Ernzerhof M., Erratum: Generalized gradient approximation made simple. *Phys. Rev. Lett.* **78,** 1396-1396(1997).

[9] Miao C. et al. Micro-nano-structured Fe_2O_3:Ti/$ZnFe_2O_4$ heterojunction films for water oxidation. *ACS Appl. Mater. Interfaces.* **4,** 4428−4433(2012).

[10] Hu L.; Peng Q.; and Li Y.; Selective Synthesis of Co_3O_4 Nanocrystal with Different Shape and Crystal Plane Effect on Catalytic Property for Methane Combustion. *J. Am. Chem. Soc.* **130**, 16136–16137 (2008).

[11] Nam K. M., Shim J. H., Han D., Kwon H. S., Kang Y., Li Y., Song H., Seo W. S., and Park J. T., Syntheses and characterization of wurtzite CoO, rocksalt CoO,and spinel Co_3O_4 nanocrystals: their interconversion and tuning of phase and morphology, *Chem. Mater.* **22,** 4446–4454(2010)

[12] Srivastava M., Selvi V. E., William G. V. K., Rajam K. S., Corrosion resistance and microstructure of electrodeposited nickel–cobalt alloy coatings. *Surface & Coatings Technology*, **201**, 3051–3060 (2006).

[13] Dinh H. T., Kuever J., Mußmann M., Hassel A. W., Widdel M. S. F., Iron corrosion by novel anaerobic microorganisms, *Nature,* **427**,829-832 (2004).

[14] Bechara R.; Balloy D.; Dauphin J. and Grimblot J.; Influence of the characteristics of γ-aluminas

on the dispersion and the reducibility of supported cobalt catalysts. *Chem. Mater.* **11**, 1703-1711(1999)

[15] Sciortino L., Giannici F., Martorana A., Ruggirello A. M., Liveri V. T., Portale G., Casaletto M. P., and Longo A., Structural characterization of surfactant-coated bimetallic cobalt/nickel nanoclusters by XPS, EXAFS, WAXS, and SAXS. *J. Phys. Chem. C.* **115**, 6360–6366(2011).

[16] Liu S., Takahashi K., Ayabe M., Hydrogen production by oxidative methanol reforming on Pd/ZnO catalyst: effects of Pd loading, *Catalysis Today, 87, 247–253(2003).*

[17] Xuan S. et al. Synthesis of Fe_3O_4@polyaniline core/shell microspheres with well-defined blackberry-like morphology. *J. Phys. Chem. C.* **112**, 18804-18809 (2008).

[18] Chang Y., Xu J., Zhang Y., Ma S., Xin L., Zhu L., and Xu C., Optical properties and photocatalytic performances of Pd modified ZnO samples, *J. Phys. Chem. C*, **113,** 18761–18767 (2009)

[19] Taratula O., Chen A. M., Zhang J., Chaudry J., Nagahara L., Banerjee I., and He H., Highly Aligned Ribbon-Shaped Pd Nanoparticle Assemblies by Spontaneous Organization, *J. Phys. Chem. C*, **111,** 7666-7670 (2007)

[20] Kootte, A., Haas, C., Groot, R. A. The electronic structure of ordered binary Co-Pt compounds. *Journal of Physics: Condensed Matter*, **3,** 1133-1152(1991).

[21] Ruban, A. V., Skriver, H. L., Nørskov, J. K. Surface segregation energies in transition-metal alloys. *Phys. Rev. B,* **59,** 15990-16000 (1999).

[22] Hirschl, R., Delbecq, F., Sautet, P., & Hafner, J. $Pt_{80}Fe_{20}$ surface from first principles: Electronic structure and adsorption of CO and atomic H. *Phys. Rev. B,* **66,** 155438(2002).

[23] Jacob, T., Goddard, W. A. Adsorption of Atomic H and O on the (111) Surface of Pt_3Ni Alloys. *J. Phys. Chem. B,* **108,** 8311-8323 (2004).

[24] Xu, Y., Ruban, A. V., Mavrikakis, M. Adsorption and Dissociation of O_2 on Pt−Co and Pt−Fe Alloys. *J. Am. Chem. Soc.* 126, 4717-4725(2004).

[25] Yuge, K., Seko, A., Kuwabara, A., Oba, F., & Tanaka, I. First-principles study of bulk ordering and surface segregation in Pt-Rh binary alloys. *Phys. Rev. B*, **74,** 174202(2006).

[26] Ma, Y., & Balbuena, P. B. Pt surface segregation in bimetallic Pt_3M alloys: A density functional theory study. *Surface Science,* **602,** 107-113(2008).

[27] Sabbe, M. K.; Lain, L.; Reyniers, M. F.; Marin, G. B. Benzene adsorption on binary Pt_3M alloys and surface alloys: a DFT study. *Phys. Chem. Chem. Phys.,* **15,** 12197(2013).